High-Temperature Materials

SCIEPublish

Article

Mullite-Corundum-Al_2TiO_5 Foamed Ceramics with Extremely Low Thermal Conductivity Induced by Multiple Thermal Resistance

Wenying Zhou [1], Lei Zhang [2], Zheng Zhang [1,3], Xiaojie Ji [1], Xingshuo Liu [1], Changcun Li [1], Jianbiao Kong [2], Penghui Du [4,*] and Degang Zhao [1,*]

[1] School of Materials Science and Engineering, University of Jinan, Jinan 250022, China; mse_zhouwy@ujn.edu.cn (W.Z.); mse_zhangz@ujn.edu.cn (Z.Z.); stu_jxj@stu.ujn.edu.cn (X.J.); mse_liuxs@ujn.edu.cn (X.L.); mse_licc@ujn.edu.cn (C.L.)
[2] Heze Institute of Product Inspection and Testing, Heze 274000, China; sdhzzl@sohu.com (L.Z.); sdhzjcy@sohu.com (J.K.)
[3] CNRS, CEMHTI UPR3079, 45000 Orléans, France
[4] State Key Laboratory of Advanced Refractories, Sinosteel Luoyang Institute of Refractories Research Co., Ltd., Luoyang 471039, China

* Corresponding author. E-mail: dupenghui072470114@163.com (P.D.); mse_zhaodg@ujn.edu.cn (D.Z.)

Received: 25 March 2026; Revised: 18 May 2026; Accepted: 29 May 2026; Available online: 10 June 2026

ABSTRACT: In the context of the global implementation of the dual carbon strategy, enhancing the thermal insulation performance of kiln insulation layers to reduce energy consumption is a highly effective route to achieving energy conservation and emission reduction. In this work, mullite foamed ceramics were fabricated via a direct-foaming method using industrial alumina and white clay as raw materials, and the thermal conductivity was decreased by introducing a secondary phase and increasing the interfacial thermal resistance. The influence of the TiO_2 addition on the phase composition, pore characteristics, and properties was systematically investigated by means of XRD, SEM, and EDS. The results indicate that the foamed ceramics are mainly composed of mullite, with minor phases including corundum and aluminum titanate. It has been demonstrated that increasing the TiO_2 addition decreased the ceramic's thermal conductivity, due to the formation of low-thermal-conductivity Al_2TiO_5 phases and the elevation of the interfacial thermal resistance. The specimen exhibiting the optimal properties is characterized by a porosity of 77.8%, a strength of 1.86 MPa, and a thermal conductivity of 0.216 W/(m·K) (1000 °C), achieved with a TiO_2 addition of 6 wt%.

Keywords: Mullite foamed ceramics; Al_2TiO_5 phase; Low thermal conductivity; Thermal insulation

1. Introduction

Mullite based foamed ceramics have been widely used in thermal insulation systems, furnace linings, electronic packaging, and energy-efficient building materials, due to their outstanding high-temperature strength, excellent thermal shock resistance, and chemical stability [1–3]. When ceramics are used in thermal insulation systems and furnace linings, low thermal conductivity is a pivotal factor in achieving

effective insulation and energy savings [4]. The thermal conductivity of ceramics is primarily governed by solid-phase conduction and thermal radiation. Introducing a high volume of porosity can effectively lower the thermal conductivity by reducing the solid-phase heat transfer. However, it inevitably compromises the mechanical properties, owing to the reduction in the effective load-bearing cross-section and the susceptibility to stress concentrations around the pores [5–8]. Consequently, the development of technical strategies to effectively reduce the thermal conductivity of mullite-based foamed ceramics while retaining mechanical properties has become a significant research focus in the field of insulation materials.

Recent studies have demonstrated that the introduction of a second phase with low solid thermal conductivity can suppress heat conduction by reducing the solid thermal conductivity [9]. Furthermore, the interfaces formed between the second phase and the matrix act as additional sites for phonon scattering, further impeding thermal transport. Notably, aluminum titanate (Al_2TiO_5) exhibits a significantly lower thermal conductivity than mullite [10–12], due to its pronounced lattice anisotropy that enhances phonon scattering [13]. Incorporating TiO_2 into a mullite matrix to form Al_2TiO_5 during the sintering process can lower the thermal conductivity by in-situ formation of a low-thermal-conductivity Al_2TiO_5 phase and an increase in mullite-Al_2TiO_5 interfaces. Furthermore, titanium dioxide, as a common additive, could promote transient liquid phase formation and accelerate sintering densification, which improves the mechanical strength of ceramics [14]. Therefore, incorporating TiO_2 into a mullite matrix provides a theoretical pathway for developing mullite ceramic materials with a lower thermal conductivity [14].

However, Al_2TiO_5 is thermally unstable at high temperatures, and its stability and quantity depend strongly on both sintering temperature and composition. Moreover, excessive TiO_2 may result in excessive liquid formation, leading to abnormal grain growth and a reduction in the compressive strength of ceramics [15]. Consequently, the relationship between TiO_2 addition, phase evolution, microstructure, and thermal conductivity should be systematically clarified to determine the optimal TiO_2 addition.

Therefore, the primary objective of this work is to systematically reveal the relationship of composition, structure, and property of the foamed ceramics tailored for industrial kiln insulation. Based on this, the present study established two strategies for achieving low thermal conductivity with a minimal loss of mechanical properties in mullite-corundum-Al_2TiO_5 composite foamed ceramics: (I) the introduction of TiO_2 for the *in-situ* formation of a low-thermal-conductivity Al_2TiO_5 phase, (II) the increase of mullite-Al_2TiO_5 interfaces. The effects of TiO_2 addition on their sintering behavior, phase evolution, and thermal conductivity were elucidated. Thermodynamic calculations using the FactSage software were employed to simulate the equilibrium phase compositions of ceramics with different TiO_2 additions to analyze the liquid-phase formation, Al_2TiO_5 generation, sintering mechanism, and heat transfer mechanism.

2. Materials and Methods

2.1. Experimental Materials

The raw materials consisted of white clay (D_{50} = 1.73 μm; Guangming Gaoke Co., Luoyang, China), industrial alumina (D_{50} = 52.28 μm; Guangming Gaoke Co., Luoyang, China), and TiO_2 powder (98.5 wt% purity, D_{50} = 20.43 μm). Their chemical compositions are listed in Table 1. Sodium alpha-olefin sulfonate (AOS, $C_{15}H_{30}SO_3Na$) and modified polyethoxylated silicone (MPS) were employed as the foaming agent and the foam stabilizer, respectively. Additionally, ammonium citrate (AC, $(NH_4)_3C_6H_5O_7$) and calcium aluminate cement (CAC; Zhengzhou Yuankai New Material Co., Ltd., Zhengzhou, China) served as the dispersant and binder, respectively. AOS, AC, and MPS were purchased from Sinopharm Chemical Reagent Co., Ltd., Shanghai, China.

Table 1. Chemical compositions of raw materials (wt%).

	SiO_2	Al_2O_3	Fe_2O_3	CaO	MgO	K_2O	Na_2O	TiO_2	IL
White clay	49.71	31.92	1.45	0.14	0.15	0.17	0.21	2.10	13.73
Industrial alumina		98.26	-	-	-	-	0.32	-	1.36
Calcium aluminate cement	0.51	76.07	0.32	19.96	0.04	0.25	0.10	0.02	1.70

2.2. Specimens Preparation

The experimental procedure is illustrated in Figure 1. First, the raw material powders, including industrial alumina, white clay, calcium aluminate cement, and TiO_2, were dry-mixed according to the formulations in Table 2. Subsequently, an initial slurry was prepared by homogeneously stirring deionized water with the dispersant (AC) for 3 min. Next, the foaming agent (AOS) and foam stabilizer (MPS) were added to this slurry and stirred rapidly for 5 min to generate the foamed slurry. The foamed slurry was then poured into molds to produce rectangular (150 mm × 40 mm × 40 mm) and disc-shaped (Φ180 mm × H20 mm) specimens for characterizing apparent porosity, bulk density, compressive strength, and thermal conductivity. After a 24-h curing period at room temperature, all specimens were dried at 110 °C for 24 h and finally sintered in an electric furnace at 1500 °C for 3 h, followed by furnace cooling to room temperature.

Table 2. Compositions of the initial slurries (wt%).

	Industrial Alumina	White Clay	TiO_2 Powder	Deionized Water	CAC	AC	AOS	MPS
T2	36.66	26.55	1.29	35.5	+4.0	+0.7	+0.5	+0.2
T4	35.91	26.01	2.58	35.5	+4.0	+0.7	+0.5	+0.2
T6	35.17	25.46	3.87	35.5	+4.0	+0.7	+0.5	+0.2
T8	34.42	24.92	5.16	35.5	+4.0	+0.7	+0.5	+0.2

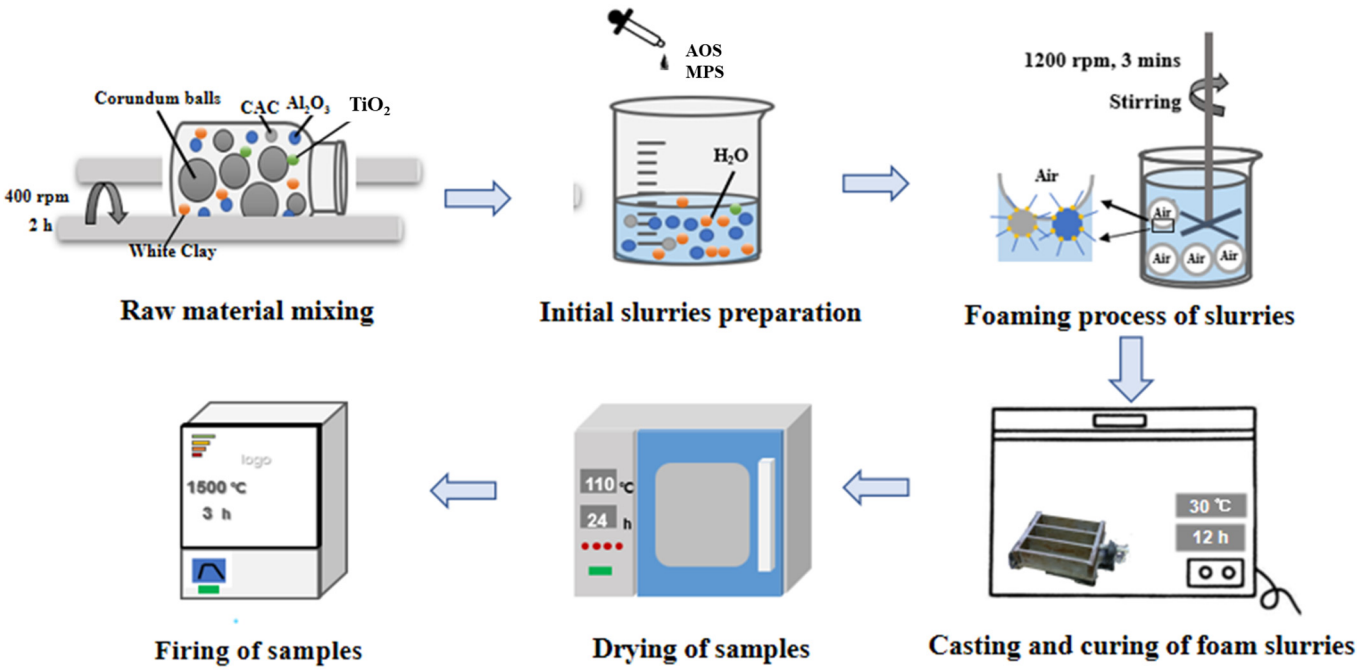

Figure 1. Schematic illustration of the experimental procedure.

2.3. Performance Characterization

The chemical compositions of the raw materials were measured by inductively coupled plasma-atomic emission spectrometry (ICP-AES) in accordance with the standard GB/T 6900-2006, while the median

particle size (D50) was determined using a laser size analyzer (Mastersizer 2000, Malvern Instruments Ltd., Malvern, UK).

The phase composition analysis was conducted via X-ray diffraction (XRD, X'pert Pro, Philips, Amsterdam, The Netherlands) with Cu Kα radiation (λ = 1.54187 Å). The data were collected in the 2θ range of 10° to 90°, at a scanning rate of 2° min^{-1}. The crystalline phases, including mullite, corundum, and aluminum titanate, were identified using the respective JCPDS cards: 01-083-1881, 00-042-1468, and 01-070-1434. The phase compositions of the specimens at 1500 °C were calculated from the Al_2O_3–SiO_2–TiO_2–CaO–MgO–Fe_2O_3–K_2O–Na_2O system, using the Equilibrium Mode of the software FactSage® (version 8.2), based on the chemical compositions in Table 1. The microstructures and elemental compositions of the samples were examined using a scanning electron microscope (SEM, JSM-6610, JEOL, Tokyo, Japan) equipped with an energy-dispersive spectrometer (EDS, QUANTAX200-30, BRUKER, Berlin, Germany). Pore size distribution was statistically evaluated from the SEM images via image analysis [16–18].

The bulk density and apparent porosity of the sintered specimens were determined by the Archimedes method, using deionized water as the immersion medium. The compressive strength of the samples was measured using a universal testing machine (ETM, Wance, Shenzhen, China) in a series of experiments. The testing was conducted at a constant loading rate of 0.05 MPa/s, ensuring a consistent and controlled testing environment. In addition, the thermal conductivity of the disc-shaped specimens was measured using a water-cooled calorimeter (PBD-30, Sinosteel Luoyang Institute of Refractories Research Co., Ltd., Luoyang, China) in compliance with the Chinese standard YB/T 4130-2005. The C_p of the samples was obtained by a mixing principle based on the heat capacity of the mullite, Al_2TiO_5, and Al_2O_3, which are extracted from the JANAF Table.

COMSOL Multiphysics was used to predict the thermal insulation behavior of foamed ceramics used in the cement rotary kiln by building a two-dimensional axisymmetric steady-state model. The model comprised a three-layer composite structure: a 5 mm steel shell (Thermal conductivity: 50 W/(m·K)), a 230 mm insulating layer, and a 115 mm working layer (spinel refractory with thermal conductivities of 0.607, 0.783, 1.037, and 1.180 W/(m·K) at 350 °C, 600 °C, 800 °C and 1000 °C). The foamed ceramics containing 2–8 wt% TiO_2 powder served as the insulating layer to assess their influence on the outer surface temperature, with their thermal conductivity values assigned according to the experimental data. Regarding boundary conditions, the internal boundary was subjected to a constant high-temperature boundary condition (T = 1450 °C), while the external boundary followed the Robin boundary condition (natural convection with ambient air at 25 °C, h = 15 W/(m^2·K)). To guarantee the maximum accuracy and reliability of the numerical results, a grid independence verification was conducted by comparing three mesh density levels (Normal, Fine, and Extremely Fine). The computed temperature discrepancy at the outer wall between the Fine and Extremely Fine profiles was negligible, confirming excellent numerical convergence. The highest-density Extremely Fine mesh model was adopted for the final steady-state heat transfer simulation.

3. Results and Discussion

3.1. Phase Composition and Microstructure

The XRD patterns and crystal phase relative compositions of the fired specimens are presented in Figure 2 and Table 3. It can be observed that mullite and corundum are the dominant crystalline phases in all samples. When the TiO_2 addition is 2 wt%, an embryonic characteristic peak of Al_2TiO_5 can be marginally detected in the magnified XRD pattern, suggesting the onset of the in-situ reaction. As the TiO_2 addition further increases to 4, 6, and 8 wt%, the diffraction peaks of Al_2TiO_5 become progressively intense, while the intensity of the corundum peaks gradually decreases, indicating that Al_2O_3 reacts with TiO_2 during

the sintering process to form the Al_2TiO_5 phase. Crucially, a closer inspection of the magnified XRD pattern in the 2θ range of 35.0°–35.5° reveals that the primary characteristic peak of mullite noticeably shifts toward higher angles with the incorporation of TiO_2. According to Bragg's law, this shift reflects a continuous shrinkage in the lattice parameters, confirming the successful solid solution of Ti^{4+} ions into the mullite matrix.

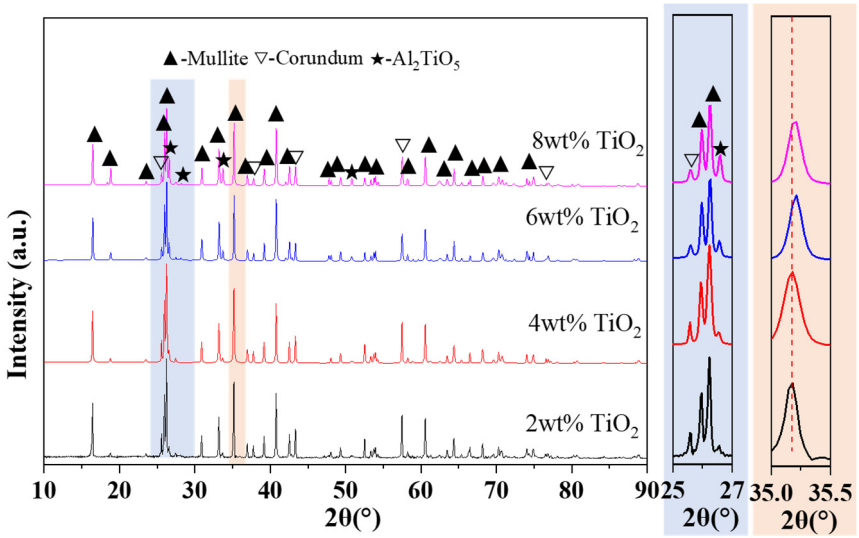

Figure 2. XRD patterns of the fired specimens with different TiO_2 additions (The blue and orange areas respectively represent the enlarged XRD diffraction patterns of 25°–27° and 35.0°–35.5°).

Table 3. Crystal phase relative compositions of the fired specimens (wt%).

TiO_2 Addition	Mullite	Corundum	Al_2TiO_5
2	63	36	1
4	59	35	5
6	70	22	8
8	67	21	12

Figure 3 and Table 4 present the microstructures and EDS results of the mullite-based foamed ceramics with varying TiO_2 additions. As shown in the micrographs, the pore walls of the specimens are primarily composed of needle-like mullite crystals, accompanied by a significant fraction of a low-melting glassy phase. Note that due to the very low content and localized high-magnification perspective, the residual corundum phase is not explicitly labeled in the SEM images, which is consistent with the weak peak intensities in the XRD patterns. With increasing TiO_2 addition, the amount of liquid phase formed during sintering gradually increases, facilitating the diffusion of Al_2O_3 and SiO_2 within the raw materials and promoting the growth of well-developed needle-like mullite crystals. Nevertheless, the grain boundaries of ceramics with 8 wt% TiO_2 addition appear rounded and less distinct, suggesting abnormal grain coarsening caused by excessive liquid-phase formation, which may adversely affect the mechanical integrity of the foamed ceramics.

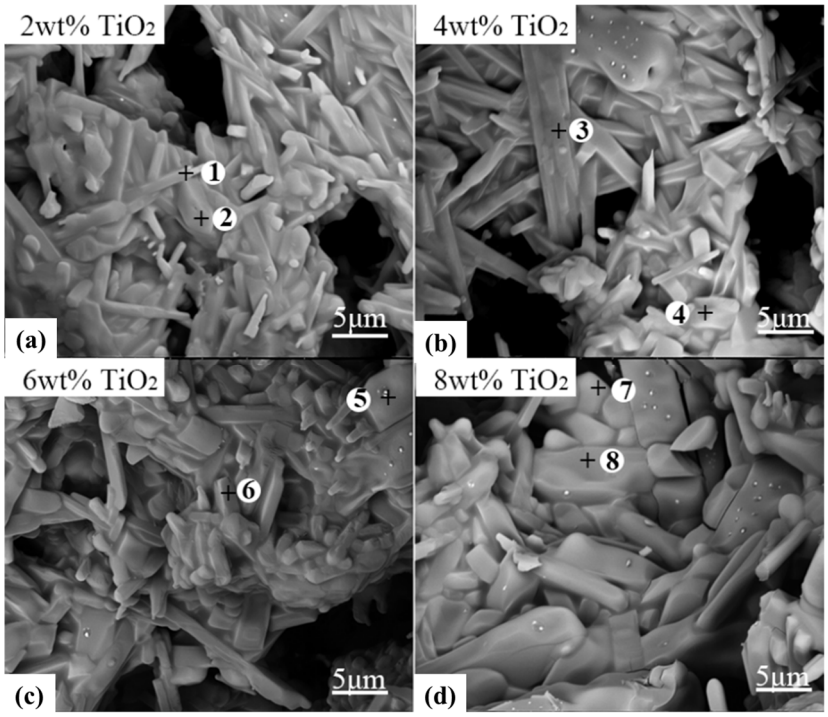

Figure 3. SEM images of specimens with various TiO_2 addition. (**a**) T2; (**b**) T4; (**c**) T6; (**d**) T8.

Table 4. EDS results of points in Figure 3 (at.%).

Point	Si	Al	O	Ti	Phase
1	10.15	28.42	60.49	0.94	Mullite
2	12.44	34.65	52.18	0.73	Mullite
3	7.68	14.53	75.06	2.73	Glass
4	6.02	22.19	68.10	3.69	Glass
5	--	11.83	80.36	7.81	Al_2TiO_5
6	7.03	17.83	72.89	2.25	Mullite
7	0.88	10.44	77.23	16.45	Al_2TiO_5
8	1.07	14.69	67.32	16.92	Al_2TiO_5

Figure 4 illustrates the statistical distributions of the geometric dimensions and aspect ratios (L/D) of mullite grains in foamed ceramics with varying TiO_2 additions. The results indicate that as the TiO_2 addition increases from 2 wt% to 6 wt%, the average length of the mullite grains is in the range from 4.9 to 5.2 μm. Correspondingly, the aspect ratio (L/D) of the grains decreases from 5.1 to 3.6. This demonstrates that within the TiO_2 adjustment range of 2–6 wt%, the network still maintains a relatively high aspect ratio, which is conducive to the formation of an interlocking columnar/acicular mullite network structure. However, when the TiO_2 addition is further increased to an excess of 8 wt%, a distinct transition in grain growth behavior is observed. The average length of the grains increases to 6.1 μm, while the aspect ratio drops sharply to 3.1. This evolutionary trend suggests that excessive TiO_2 facilitates the abundant formation of a liquid phase and reduces its viscosity, shifting the grain growth from anisotropic longitudinal elongation to coarsening growth, thereby suppressing the development of high-aspect-ratio acicular mullite.

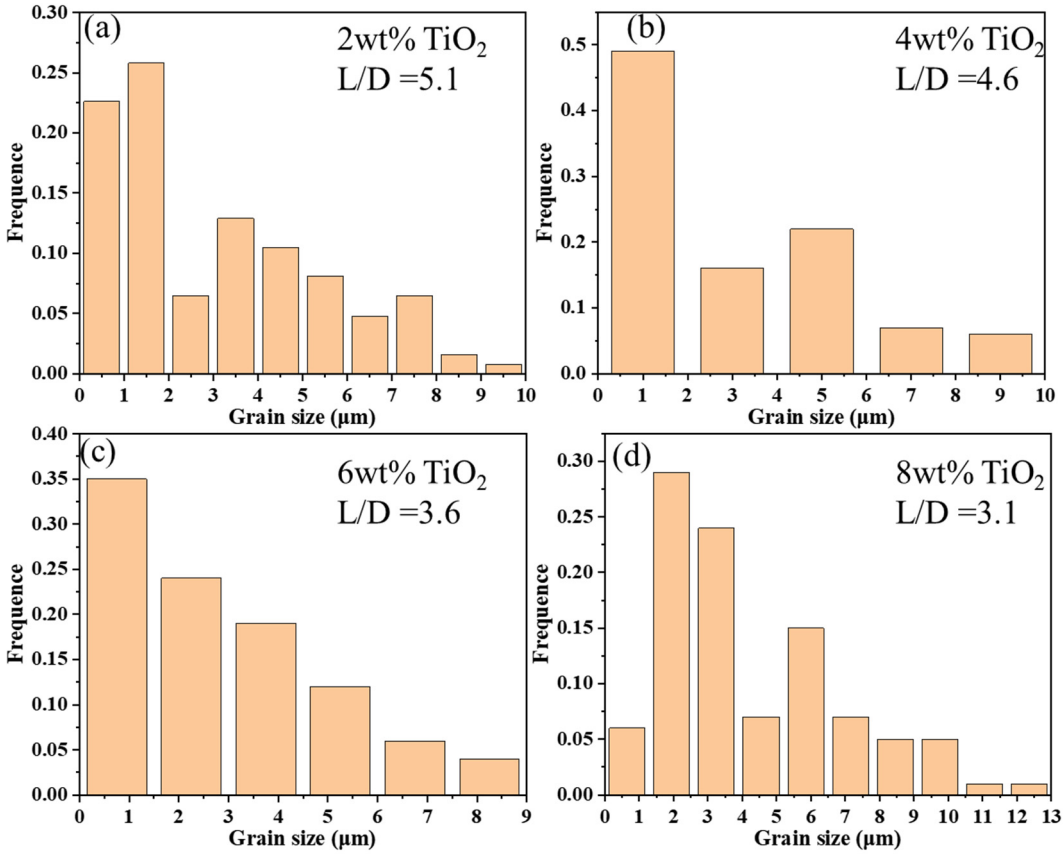

Figure 4. The statistical distribution of the geometric dimensions and aspect ratios (L/D) of mullite grains of foamed ceramics in varying TiO_2 addition. (**a**) T2; (**b**) T4; (**c**) T6; (**d**) T8.

To deeply elucidate the effect of TiO_2 addition on the phase evolution, thermodynamic calculations were performed using FactSage 8.2, and the theoretical phase assemblages at different temperatures are shown in Figure 5. For the sample with 2 wt% TiO_2 (Figure 5a), impurities in the raw materials reacted to form a transient liquid phase, which facilitated ionic diffusion and accelerated sintering. With increasing temperature to 1300 °C, TiO_2 in the white clay reacts with alumina to form a small amount of Al_2TiO_5. However, this phase is thermally unstable and tends to decompose at higher temperatures. Consequently, upon sintering at 1500 °C, the Al_2TiO_5 phase diminishes and contributes to additional liquid formation, consistent with the absence of Al_2TiO_5 reflections in the XRD patterns (Figure 2). With increasing TiO_2 addition to 8 wt%, a larger fraction of Al_2TiO_5 forms at the expense of corundum and TiO_2, thereby reducing the corundum content and inhibiting mullite formation (Figure 5e). Notably, the TiO_2 addition exerts a limited effect on the overall liquid fraction but significantly reduces the liquid viscosity (Figure 5f), thereby enhancing mass transport and promoting densification. Nevertheless, excessive TiO_2 leads to overly fluid liquid phases, resulting in exaggerated grain growth and abnormal microstructural coarsening, in agreement with the microstructure of the ceramics shown in Figure 3.

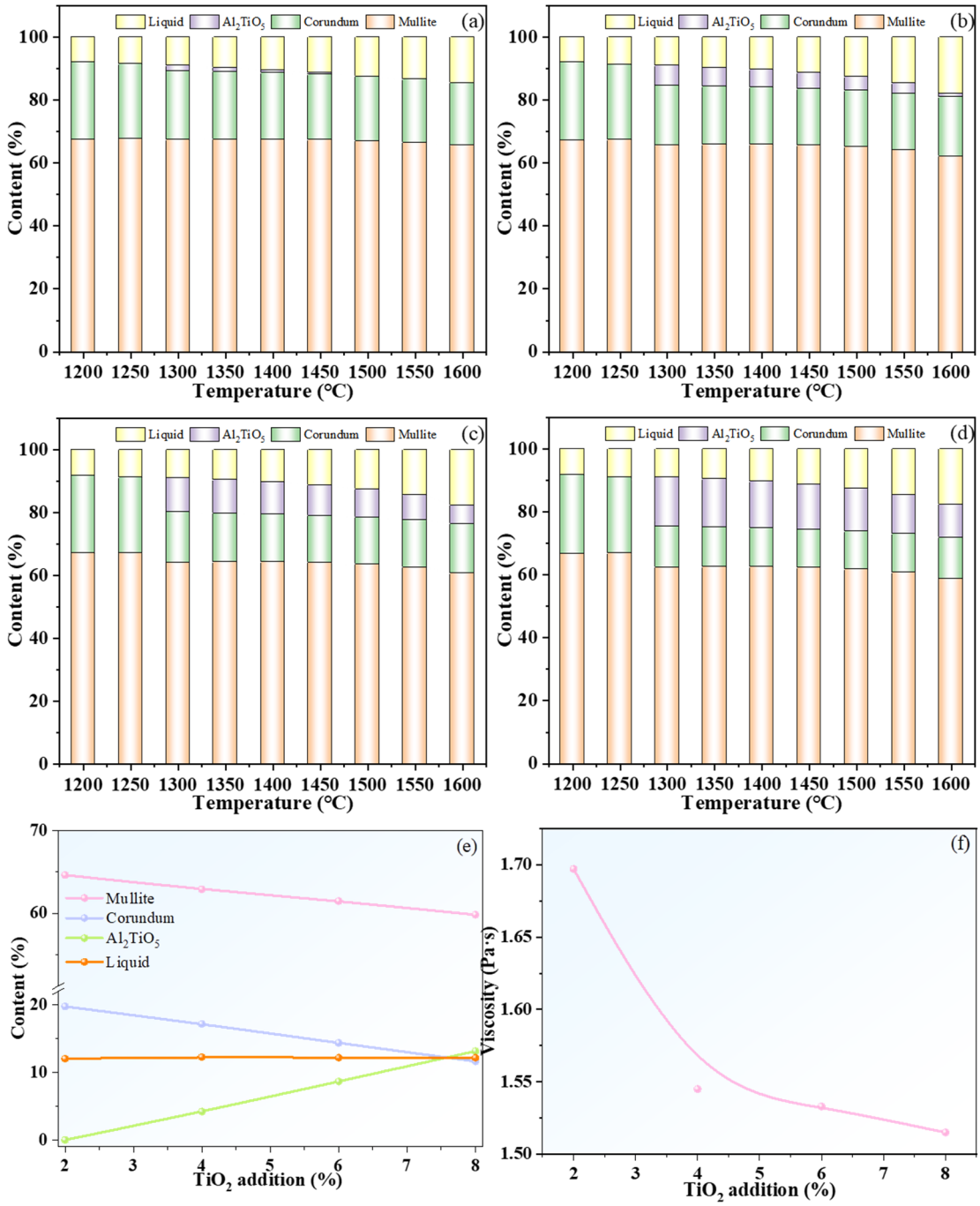

Figure 5. The theoretical phase composition of ceramics calculated by thermodynamic software Factsage 8.2: (**a**) T2, (**b**)T4, (**c**)T6, (**d**)T8, (**e**) Phase composition of ceramics with different TiO_2 additions at 1500 °C, (**f**) Liquid viscosity.

3.2. Pore Characteristics of the Specimens

To investigate the correlation between TiO_2 addition and the pore structure, the fractal dimension, pore size, and morphology of the specimens were analyzed using ImageJ software (Version Fiji), and the results are presented in Figure 6. The fractal dimension (D), which reflects the complexity and irregularity of the pore shape [19,20], exhibits only minor variation with TiO_2 addition, ranging between 1.675 and 1.704 (Figure 6a–d), implying that TiO_2 addition has a limited influence on pore geometry. All specimens exhibited a bimodal pore size distribution, composed of intra-strut pores (0–10 μm) and inter-strut pores (50–400 μm), as illustrated in Figure 6e,f. As the TiO_2 content increases from 2 to 8 wt%, the peak intensity associated with the inter-strut pores shows a progressive increase, while peak intensity for the intra-strut

pores decreases. This is attributed to the increased liquid-phase content and enhanced sintering densification with higher TiO_2 addition, which effectively reduce intra-strut pores resulting from particle accumulation within the pore walls. Furthermore, the median pore diameter decreases from 219 μm to 190 μm as TiO_2 addition increases from 2 wt% to 6 wt%, before slightly increases to 201 μm at 8 wt%.

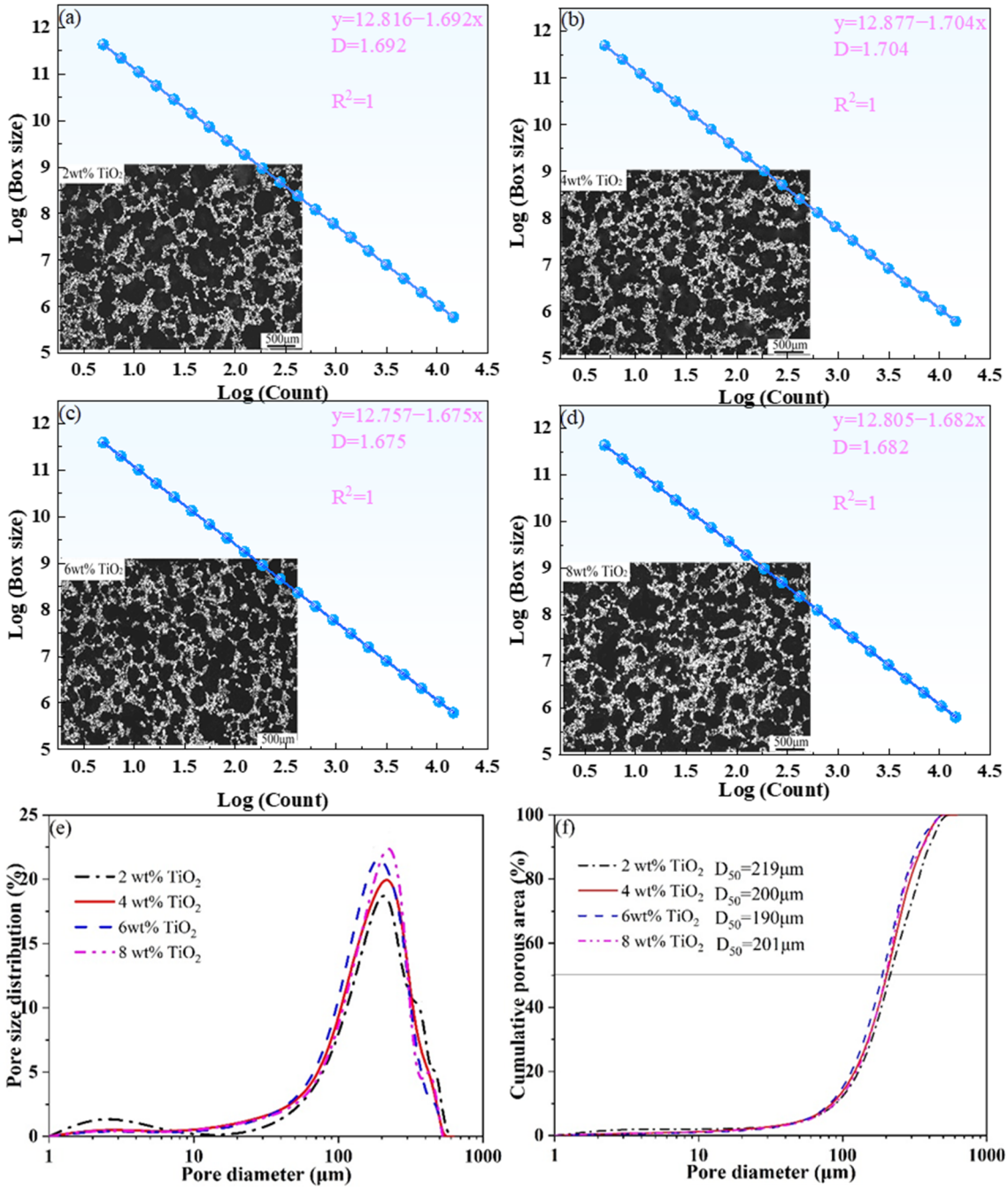

Figure 6. Fractal dimension (**a**–**d**) and pore size distribution curves (**e**,**f**) of fired specimens with various TiO_2 additions.

3.3. Properties of the Fired Specimens

A summary of the physical properties characterizing the sintered specimens is presented in Table 5. With an increase in TiO_2 addition from 2 wt% to 8 wt%, the apparent porosities, bulk densities, and compressive strengths of specimens remain relatively stable. The porosities are in the range of 77.8–78.8%, while the compressive strengths range from 1.67 to 1.86 MPa.

Table 5. Properties of the fired specimens with various TiO_2 additions.

TiO_2 Addition (wt%)	Linear Shrinkage Rate (%)	Apparent Porosity (%)	Bulk Density (g/cm^3)	Compressive Strength (MPa)
2	4.94 ± 0.12	78.8 ± 0.3	0.68 ± 0.01	1.67 ± 0.04
4	5.42 ± 0.23	78.4 ± 0.6	0.68 ± 0.01	1.75 ± 0.10
6	5.70 ± 0.18	77.8 ± 0.3	0.72 ± 0.01	1.86 ± 0.15
8	7.41 ± 0.15	78.8 ± 0.2	0.68 ± 0.01	1.78 ± 0.06

Figure 7 shows the thermal conductivity of the fired specimens as a function of temperature. A consistent reduction in thermal conductivity is observed with increasing TiO_2 addition at any given temperature. Notably, at 350 °C, the value decreases from 0.202 W/(m·K) to 0.123 W/(m·K) as the TiO_2 addition increases from 2 wt% to 8 wt%. When a small amount of TiO_2 (<4 wt%) is introduced, Ti^{4+} ions enter the mullite lattice through cation substitution, generating a limited number of point defects and local strain fields within the ceramic matrix (Figure 5). These structural disturbances enhance phonon scattering and consequently reduce the thermal conductivity of the ceramics. In this time, the ceramics provide a primary thermal conduction path through mullite-corundum via path 1 (shown in Figure 8). As TiO_2 addition further increases to 8 wt%, TiO_2 reacts with alkali oxide impurities in the white clay to form Al_2TiO_5 and liquid phases (Figure 5) with a lower thermal conductivity. This significantly increases the complexity of the phonon scattering path, creating intricate interfaces such as mullite-corundum, corundum-Al_2TiO_5, and corundum-Al_2TiO_5-liquid (Path 2: mullite-corundum-Al_2TiO_5-liquid-mullite-liquid and their interfaces, shown in Figure 8), which elevates the interfacial thermal resistance during heat transfer. Therefore, the thermal conductivity of ceramics decreases significantly [10,11].

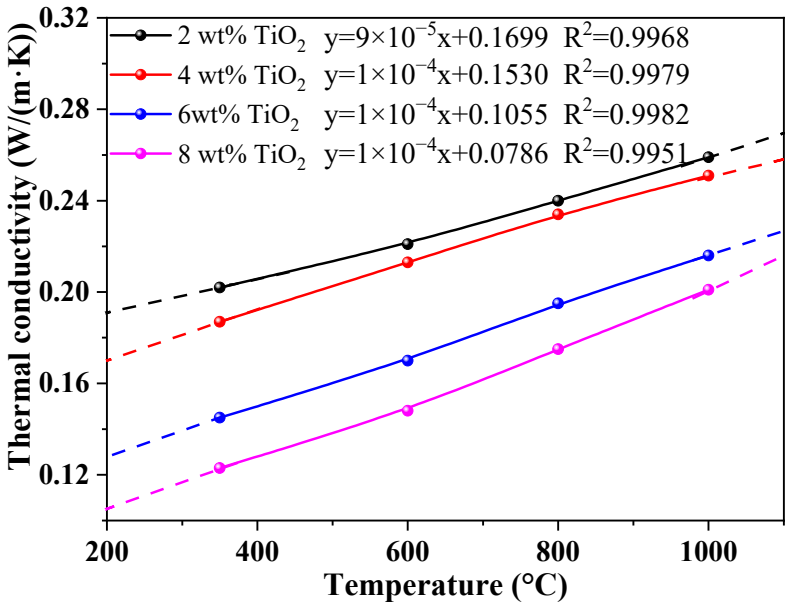

Figure 7. Thermal conductivities of the four specimens with TiO_2 addition at varying testing temperature.

The thermal conductivity of all specimens increases monotonically with the testing temperature. The maximum value of 0.259 W/(m·K) is observed at 1000 °C for the specimen containing 2 wt% TiO_2. Heat transfer in porous ceramics is governed by coupled mechanisms of solid conduction, gaseous conduction, and thermal radiation [21–23]. For the foamed ceramics at low temperatures, heat transport is primarily dominated by phonon conduction through the mullite struts; however, the incorporation of TiO_2 introduces additional lattice defects and complex pore-wall interfaces, which significantly enhance phonon scattering and result in a relatively low thermal conductivity. As the temperature increases, gas-phase conduction and

thermal radiation become more prominent, leading to a more pronounced acceleration in the effective thermal conductivity.

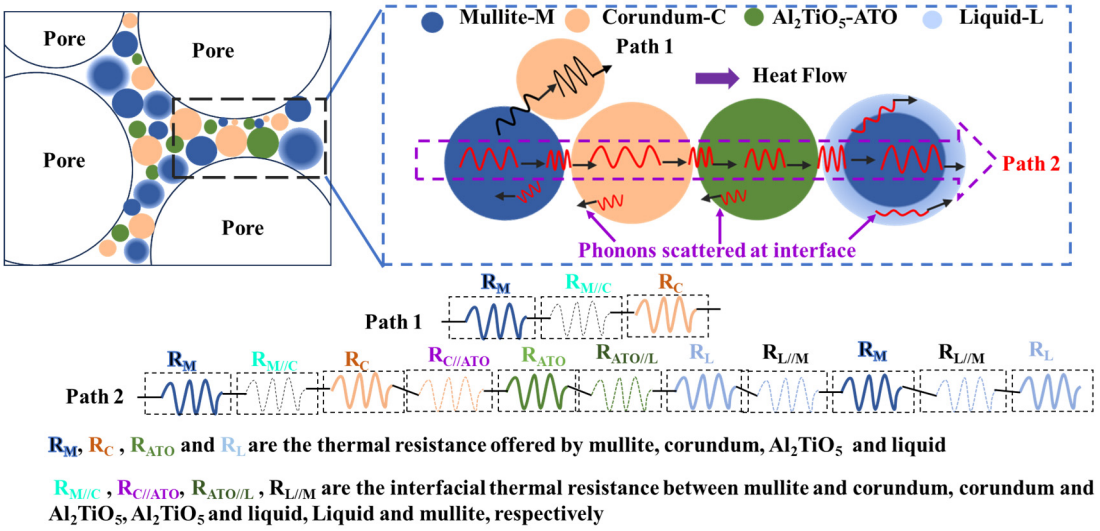

Figure 8. Schematic showing effective thermal resistance circuits for mullite-corundum-Al_2TiO_5 foamed ceramics.

3.4. The Application of Ceramics in Industrial Kilns

In foamed ceramics for thermal insulation, apparent porosity (P), compressive strength (σ), and bulk density are of vital importance. Furthermore, the thermal resistivity (defined as the reciprocal of the thermal conductivity, 1/λ) and heat storage capacity (ρC_p) are crucial for evaluating the thermal performance. To better understand the properties of foamed mullite ceramics, a radar map was plotted based on the properties mentioned above, as shown in Figure 9. It can be seen from this figure that TiO_2 addition has a limited influence on the compressive strength of ceramics, but affects their thermal conductivity significantly. With increasing TiO_2 addition from 2 to 6 wt%, both the compressive strength and thermal insulating properties are improved. Further increasing the TiO_2 addition to 8 wt%, the thermal insulating performance is efficiently enhanced, but the mechanical properties deteriorate. To further elucidate the thermal insulating properties of ceramics, the finite element software COMSOL Multiphysics (Version 6.2) was used to simulate the temperature field of the furnace lining.

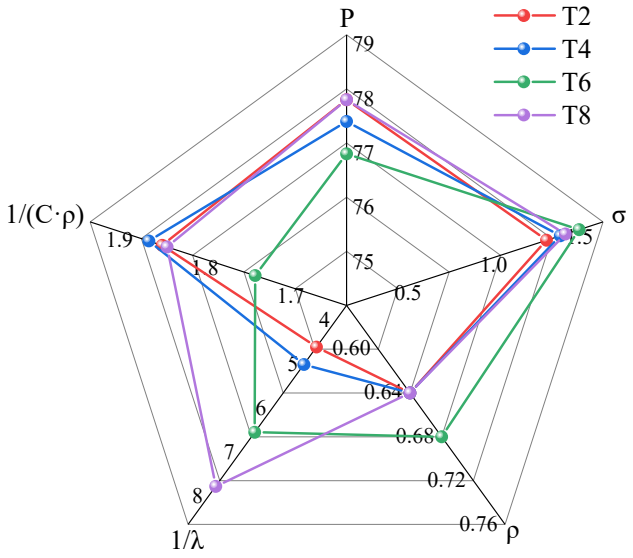

Figure 9. Radar map exhibiting the thermal insulation performance.

The temperature distribution of the kiln wall in a cement rotary kiln was calculated using a two-dimensional (2D) steady-state model in COMSOL Multiphysics, and the results are shown in Figure 10. The semicircular cross-section in Figure 10a represents the kiln wall structure, consisting of the high-temperature working layer, the thermal insulation ceramic layer, and the metal shell from the inside to the outside, with a typical radial heat-conduction profile. Figure 10b shows the temperature field distribution across the kiln wall. As can be observed, when T8 ceramic is used as the insulation layer, the outer surface temperature of the kiln wall is 75.9 °C, indicating that the T8 ceramic possesses excellent thermal insulation performance. It effectively reduces heat loss through the kiln wall, maintaining a low external surface temperature, thereby improving both the energy efficiency and operational safety of the kiln.

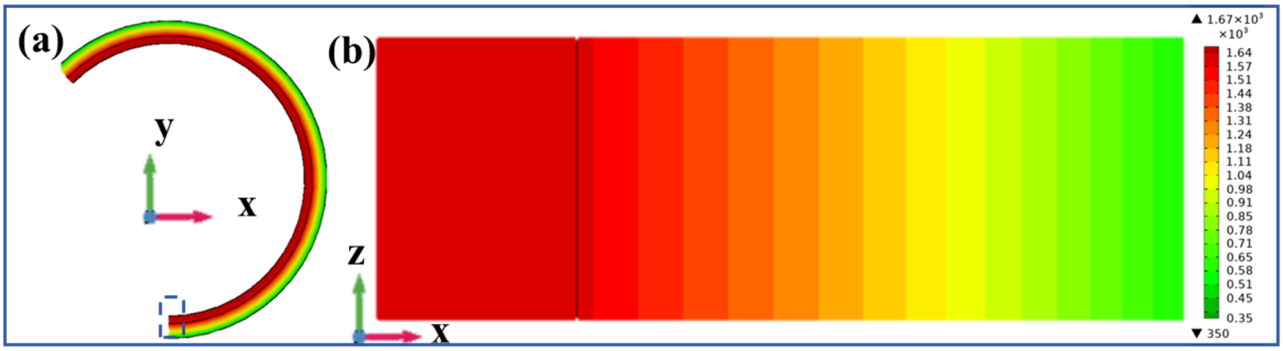

Figure 10. The 2D steady-state calculation results by COMSOL: (**a**) wall structure of the kiln and (**b**) temperature field distribution across the kiln wall.

Based on the COMSOL simulation results, the temperature gradient distribution (Figure 11a) and the outer surface temperature (Figure 11b) of the kiln lining were obtained. As shown in Figure 11a, the choice of insulation materials significantly influences the outer surface temperature. When T2, T4, T6, and T8 ceramics are employed as the insulation layers, the corresponding outer wall temperatures of the kiln are 96.7 °C, 93.5 °C, 82.2 °C, and 75.9 °C, respectively, indicating that the introduction of TiO_2 effectively enhances the thermal insulation performance of the materials and exhibits excellent application potential in industrial kiln and furnace systems.

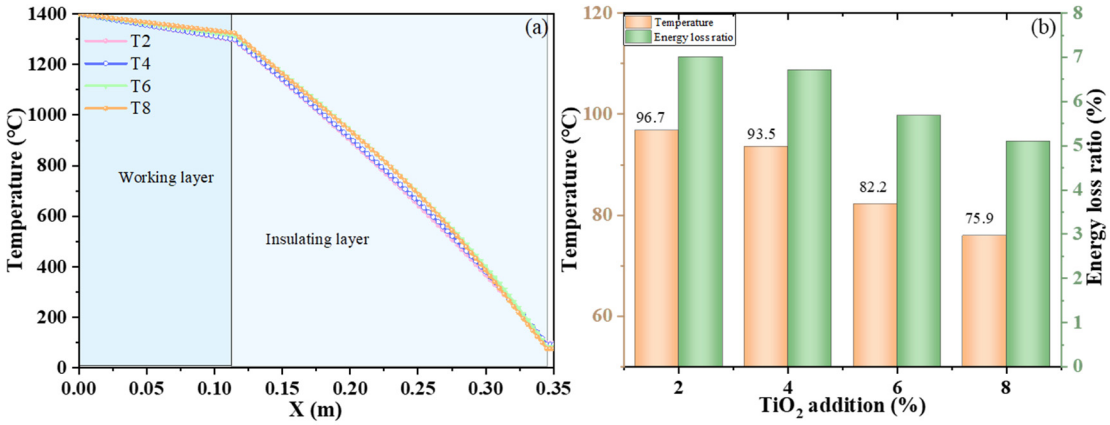

Figure 11. (**a**) The temperature gradient distribution and (**b**) The outer surface temperature.

Based on the heat flow, the thermal energy loss was calculated to reveal a strong dependence on the type of insulation material employed. Assuming the length of the kiln is 74 m, the calculated hourly energy loss results of the kiln with different insulating layers (T2–T8) were 2100 kW, 2014 kW, 1703 kW, and 1530 kW, exhibiting a systematic decline, which is attributable to the reduced conductive heat transfer

across the insulation layer. The energy loss ratio shows a similar tendency, decreasing from 7.0% to 5.1%. Compared with the T2 insulation, the best-performing sample (T6) reduces energy loss by approximately 397 kW, which translates into a natural gas saving of about 37.5 m^3 and a reduction in CO_2 emissions of nearly 71 kg over the same period. If the kiln operates 360 days per year, it is estimated that approximately 2.7×10^5 m^3 of natural gas can be conserved, accompanied by a reduction of about 512 t in CO_2 emissions. This decrease in energy dissipation directly lowers the demand for natural gas combustion, thereby reducing not only the operational energy input but also the environmental footprint of the process.

Furthermore, it is essential to discuss the long-term thermal stability of the *in-situ* formed Al_2TiO_5 phase under actual service conditions, given its intrinsic thermodynamic decomposition tendency within 900–1280 °C. In this composite system, the potential degradation or failure of the material is expected to be effectively mitigated by two factors. The limited solid solution of silicon/mullite species within the Al_2TiO_5 lattice can increase the activation energy required for its decomposition, thereby enhancing its thermodynamic stability. Microstructurally, the fine Al_2TiO_5 grains are highly dispersed and locked within the rigid framework of interlocking mullite crystals. This matrix encapsulation provides strong spatial constraints, which suppress microcrack initiation even when micro-volume fluctuations occur during long-term heat preservation. Given that industrial kiln insulation layers mostly experience steady-state thermal profiles rather than drastic thermal shocks, the mullite-corundum-Al_2TiO_5 foamed ceramics are expected to exhibit sufficient long-term stability for industrial applications.

4. Conclusions

In this study, mullite-based foamed ceramics with low thermal conductivity were successfully fabricated via a direct foaming method. The influence of TiO_2 addition on the phase evolution, microstructure, and thermophysical properties was systematically elucidated. The main conclusions are summarized as follows:

(1) The sintered foamed ceramics are primarily composed of mullite, with minor phases of corundum and *in-situ* aluminum titanate. Thermodynamic simulations reveal that TiO_2 addition effectively reduces liquid-phase viscosity, thereby promoting the development of needle-like mullite crystals and matrix densification.
(2) TiO_2 addition has a limited impact on apparent porosity and compressive strength. However, it significantly reduces the thermal conductivity. This reduction is attributed to two synergistic mechanisms: enhanced phonon scattering induced by lattice defects and a substantial increase in interfacial thermal resistance across the complex mullite-corundum-Al_2TiO_5 interfaces.
(3) The specimen with 6 wt% TiO_2 addition exhibits the most favorable balance of properties, maintaining a high porosity of 77.8% and a compressive strength of 1.86 MPa, while achieving a low thermal conductivity of 0.216 W/(m·K) at 1000 °C.
(4) The simulations demonstrate that employing these foamed ceramics as an insulating layer can reduce the outer shell temperature of a rotary kiln. This underscores the significant potential of these materials for enhancing energy efficiency and operational safety in high-temperature industrial furnace systems.

Author Contributions

Methodology, W.Z.; Investigation, W.Z., L.Z. and Z.Z.; Writing—Original Draft Preparation, W.Z.; Data Curation, W.Z., X.J., J.K. and P.D.; Writing—Review & Editing, W.Z. and C.L; Supervision, D.Z.; Project Administration, W.Z., D.Z. and X.L.; Funding Acquisition, D.Z.

Ethics Statement

Not applicable.

Informed Consent Statement

Not applicable.

Data Availability Statement

The data are available from the corresponding author on reasonable request.

Funding

This research was funded by the Natural Science Foundation of Shandong Province (Nos. ZR2025QC605 and ZR2024QE044), Opening Fund of State Key Laboratory of Advanced Refractory Materials (NO. SKLAR202411), Shandong Provincial Key Research and Development Program (No. 2025CXGC020107), the Innovation Capacity Improvement Project for Technology-based Small and Medium Enterprises in Shandong Province (No. 2024TSGC0788), and Jinan City-School Integration Development Strategy Project (Nos. JNSX2023015 and JNSX2023018).

Declaration of Competing Interest

The authors declare that they have no known competing financial interests or personal relationships that could have appeared to influence the work reported in this paper.

References

1. Zhang Z, Zhou WY, Han BQ, Li YB, Yan W, Xu NN, et al. Preparation and characterization of eco-friendly and low-cost mullite-corundum foamed ceramics with low thermal conductivity. *Ceram. Int.* **2019**, *45*, 13203–13209. DOI:10.1016/j.ceramint.2019.04.003
2. Ji X, Wang W, Bo L, Liu X, Li C, Zhang Z, et al. A rapid solidification preparation of alumina-based foamed ceramics with high mechanical properties. *Ceram. Int.* **2025**, *51*, 55240–55249. DOI:10.1016/j.ceramint.2025.09.246
3. Zhou W, Zhang Z, Li N, Yan W, Ye G. A new mullite foamed ceramic prepared by direct-foaming methods in parallel with a mechanical activation technique. *Ceram. Int.* **2022**, *48*, 20721–20730. DOI:10.1016/j.ceramint.2022.04.053
4. Zhou W, Yan W, Li N, Li Y, Dai Y, Han B, et al. Preparation and characterization of mullite foam ceramics with porous struts from white clay and industrial alumina. *Ceram. Int.* **2018**, *44*, 22950–22956. DOI:10.1016/j.ceramint.2018.09.092
5. Uyanna O, Najafi H. Thermal protection systems for space vehicles: A review on technology development, current challenges and future prospects. *Acta Astronaut.* **2020**, *176*, 341–356. DOI:10.1016/j.actaastro.2020.06.047
6. Luo Y, Wu YH, Ma SH, Zheng SL, Chu PK. An eco-friendly and cleaner process for preparing architectural ceramics from coal fly ash: Pre-activation of coal fly ash by a mechanochemical method. *J. Clean. Prod.* **2019**, *214*, 419–428. DOI:10.1016/j.jclepro.2018.12.292
7. Zhou X, Xu Y, Chen Y, Tian F. Mechanism on lattice thermal conductivity of carbon-vacancy and porous medium entropy ceramics. *Scripta Mater.* **2025**, *259*, 116568. DOI:10.1016/j.scriptamat.2025.116568
8. Majeed A, Ali P, Kouki M. Single and multi-walled carbon nanotubes with radiative heat transfer over a porous medium: Featuring of darcy–forchheimer and thermal conductivity. *Nano-Struct. Nano-Objects* **2024**, *40*, 101416. DOI:10.1016/j.nanoso.2024.101416
9. Zhao Y, Sun X, Guo R, Liu H, Zhao X, Huo M, et al. Lightweight Y_2O_3 stabilized ZrO_2 (YSZ) fiber porous ceramics with ultra-low thermal conductivity. *Ceram. Int.* **2025**, *51*, 29187–29196. DOI:10.1016/j.ceramint.2025.04.124
10. Duan J, Han B, Wei J, Yu H, Li N, Li Y, et al. Preparation and characterization of Al_2TiO_5 ceramics with low thermal conductivity: Role of alumina sources. *J. Aust. Ceram. Soc.* **2025**, *61*, 1601–1611. DOI:10.1007/s41779-025-01195-y
11. Jiang M, Shi C, Liu Y, Li X, Deng T. Microcosmic analysis of stabilization of aluminum titanate ceramics by mg migration into the Al_2TiO_5 lattice. *Ceram. Int.* **2025**, *51*, 43637–43648. DOI:10.1016/j.ceramint.2025.07.096
12. Xu J, Guo Y. Uncovering the roughness effect on inelastic phonon scattering and thermal conductance at interface via spectral energy exchange. *Int. J. Heat Mass Transf.* **2025**, *250*, 127295. DOI:10.1016/j.ijheatmasstransfer.2025.127295
13. Sun M, Quan X, Ma X, Chen H, Qin X, Zhou G. Effects of TiO_2 doping and sintering temperature on electrical, mechanical and thermal properties of Al_2O_3 ceramics. *Ceram. Int.* **2025**, *51*, 61013–61024. DOI:10.1016/j.ceramint.2025.10.296
14. Ma B, Zan W, Fan W, Yu C, Liu H, Deng C, et al. Influence of Al_2TiO_5 on the sintering properties and thermal shock resistance of Y_2O_3-based refractories. *Ceram. Int.* **2025**, *51*, 50290–50301. DOI:10.1016/j.ceramint.2025.08.262

15. Liu Y, Guo WM, Lin HT, Liang S, Lu YJ, Wang HL. Low-temperature preparation and enhanced mechanical properties of (Ti, Zr, Nb, Ta, Mo)C composites via $CoSi_2$ liquid-phase sintering. *J. Alloys Compd*. **2025**, *1041*, 183816. DOI:10.1016/j.jallcom.2025.183816
16. Zhou W, Yan W, Li N, Li Y, Dai Y, Zhang Z. Fabrication and characterization of a mullite-foamed ceramic reinforced by *in-situ* SiC whiskers. *Ceram. Int.* **2020**, *46*, 3132–3138. DOI:10.1016/j.ceramint.2019.10.016
17. Zhou W, Ma Z, Ye G, Yuan B, Zhang Z, Zhao D. Optimizing the pore structure and properties of alumina-based foamed ceramics through curing condition prioritization. *J. Alloys Compd*. **2025**, *1022*, 180065. DOI:10.1016/j.jallcom.2025.180065
18. Zhou W, Ma Z, Ye G, Li H, Zhang Z, Zhao D. Synergistic enhancement of mechanical strength and thermal insulation in alumina foamed ceramics: Role of silica fume nucleation in curing process and sintering mechanism. *Ceram. Int.* **2025**, *51*, 26204–26212. DOI:10.1016/j.ceramint.2025.03.303
19. Liu Z, Gao J, Tian C, Zhang D, Peng Z, Zhang L, et al. Preparation and study of mullite ceramic fibre porous membranes with near-net shape forming and high gas permeability. *Ceram. Int.* **2025**, *51*, 2626–2638. DOI:10.1016/j.ceramint.2024.11.246
20. Jodha KS, Salazar Marocho SM, Mecholsky JJ, Lirette ST, Duan Y, Griggs JA. Comparing four different methods of measuring fracture toughness and its relationship with fractal dimension in a polycrystalline (3Y-TZP) dental ceramic. *Dent. Mater.* **2025**, *41*, 425–431. DOI:10.1016/j.dental.2025.01.002
21. Fu B, Sun Y, Jiang W, Wang F, Zhang L, Wang H, et al. Determining the thermal conductivity and phonon behavior of SiC materials with quantum accuracy via deep learning interatomic potential model. *J. Nucl. Mater*. **2024**, *591*, 154897. DOI:10.1016/j.jnucmat.2024.154897
22. Nguyen VT, Nguyen VH, Naili S. Deep learning-based multiscale prediction of composite aerogels' effective thermal conductivity. *Int. J. Mech. Sci*. **2025**, *304*, 110617. DOI:10.1016/j.ijmecsci.2025.110617
23. Wang Q, Gui N, Yang X, Tu J, Jiang S. The effects of grain size and fractal porosity on thermal conductivity of nano-grained graphite: A molecular dynamics study. *Int. J. Heat Mass Tran*. **2024**, *220*, 125030. DOI:10.1016/j.ijheatmasstransfer.2023.125030